Journal of Magnetism and Magnetic Materials 491 (2019) 165557

Contents lists available at ScienceDirect

Journal of Magnetism and Magnetic Materials

journal homepage: www.elsevier.com/locate/jmmm

Research articles

Anisotropic spin-wave dispersion in two-dimensional $Ni_{80}Fe_{20}$ diatomic nanodot array

Anulekha De[a], Chandrima Banerjee[a], Avinash Kumar Chaurasiya[a], Ruma Mandal[a], Yoshichika Otani[b,c], Rajib Kumar Mitra[d], Anjan Barman[a,*]

[a] Department of Condensed Matter Physics and Material Sciences, S. N. Bose National Centre for Basic Sciences, Salt Lake, Block JD, Sector III, Kolkata 700106, India
[b] Institute for Solid State Physics, University of Tokyo, 5-1-5 Kashiwanoha, Kashiwa, Chiba 277-8581, Japan
[c] RIKEN-CEMS, 2-1 Hirosawa, Wako, Saitama 351-0198, Japan
[d] Department of Chemical, Biological and Macromolecular Sciences, S. N. Bose National Centre for Basic Sciences, Salt Lake, Block JD, Sector III, Kolkata 700106, India

ARTICLE INFO

Keywords:
Diatomic nanodot array
Brillouin light scattering (BLS)
Plane wave method (PWM)
Micromagnetic simulations
Magnonic band structure
Spin-wave dispersion
Iso-frequency contours

ABSTRACT

Artificially patterned magnonic crystals serve as a promising candidate for the emerging research fields of magnonics and spintronics. Here, we investigate the spin-wave dispersion in a diatomic nanodot lattice made of $Ni_{80}Fe_{20}$ nanodots of two different diameters placed in close proximity to form a binary magnonic crystal with a complex double-dot unit cell. The frequency dispersion of SW eigenmodes experimentally measured by the Brillouin light-scattering technique is in good agreement with the numerically calculated band structure derived from the linearized Landau-Lifshitz equation. Due to the change of the nature of interaction among the dots in two mutually perpendicular orientation of the applied bias magnetic field, magnonic band structure, including the slope of the dispersion curves, varies significantly. The anisotropic SW propagation is also studied numerically by local excitation of spin-wave dynamics in this system. This phenomenon is further explained by the calculated iso-frequency contours. Efficient manipulation of spin waves in this new type of two-dimensional magnonic crystal is promising for the development of nanoscale magnonic and spintronic devices.

1. Introduction

The rapid development in the emerging research field of 'magnonics' and 'magnon-spintronics' is connected to the possibility of using spin waves (SWs) as means for low power signal transmission and data processing. Recently, magnetic nanostructures have emerged as a promising candidate in the fields of spin-torque- (ST-) and spin-Hall nano-oscillators (SHNO) [1,2] and magnonic crystals (MCs) [3,4], in addition to their conventional usage in magnetic storage, memory and sensor devices. The MCs represent the magnetic counterpart of photonic, phononic and plasmonic crystals offering unprecedented opportunity to design and exploit new generation GHz-frequency logic devices [5], filters [6], phase shifters [7], couplers [8], transistors [9] and high-sensitivity magnetic sensors [10]. Magnonic devices offer better prospects for miniaturization as SWs operating at GHz or sub-THz frequencies have micrometric or nanometric wavelength. Knowledge of the nature of SW propagation and magnonic band structure of any MC is essential to any desired application.

A range of theoretical and experimental studies have surged during last one decade, which continue to grow at a fast pace on the tailoring of magnonic spectra and band structure in one- [11,12], pseudo-one [13], two- [14–17], and three-dimensional [18,19] arrays of magnetic nanostructures. Recently, efficient control over the magnonic band structure in dense arrays of width-modulated permalloy nanowires have been reported [20]. Initial works on SW quantization and propagation in ferromagnetic nanodot arrays showed neither dispersive modes nor magnonic band gap formation [21,22]. The SW dynamics in those systems were mainly governed by the internal fields of the nanodots and dipolar interactions between the nanodots. Afterwards, a few experimental studies showed the evidence of dispersive nature and propagating character of SW modes in two-dimensional arrays of closely packed nanodots. Considerable anisotropy concerning the dynamical coupling and the existence of maxima and minima in the dispersion curves of the propagating SWs for different bias magnetic field orientations has been observed in some nanodot arrays of square and hexagonal symmetry [23–25]. More recently, Graczyk *et al.*, demonstrated the magnonic band structure and formation of hybridization and Bragg bandgap in a continuous permalloy film induced by vertical dynamic coupling with an array of permalloy/Pt nanodots [26].

Newer and more complex structures are nowadays being introduced

* Corresponding author.
E-mail address: abarman@bose.res.in (A. Barman).

https://doi.org/10.1016/j.jmmm.2019.165557
Received 30 May 2019; Accepted 9 July 2019
Available online 13 July 2019

for better functionalities and tunable properties. These include bi-component magnonic crystals (BMCs) [27–30] and magnonic quasi-crystals [31,32] which provide more control parameters for tuning the magnonic bands. Nonetheless, the improved device operations necessitate more complex fabrication processes, including multistep lithography and two-photon photolithography. Binary magnonic crystal (BMN) is another type of complex magnonic crystal, which can be fabricated using simpler lithographic technique by placing two different structures of the same material next to each other forming a complex base. Hitherto, very few works have been reported on such structures. BMN in the form of anti-ring or annular antidot lattice, showed some new modes due to the interaction between the antidot and the central dot regions [33,34]. Another new structure has been reported where two antidot sublattices of alternating diameters create non uniform demagnetizing field which significantly alters the field dependent SW mode transformation [35].

Recently, we have introduced a new type of BMN in the form of a diatomic nanodot lattice where two nanodots of different sizes are placed in close proximity to each other. We have reported the bias-field-dependent resonant modes and their spatial profiles at $q \approx 0$ wave vector and observed the effect of the double-dot unit cell in its field dependent SW spectra [36]. In the present study, we have investigated both experimentally and numerically how the complex double-dot unit cell engineers the SW dispersion with wave vector in two orthogonal orientations of the bias magnetic field. The calculated *iso*-frequency contours explain the origin of anisotropic propagation of some of the eigenmodes. Achievement of band tunability in such complex structure by simply changing the bias field orientation is useful for practical implementation.

2. Experimental details

A 30-nm-thick circular shaped $Ni_{80}Fe_{20}$ (permalloy, Py hereafter) diatomic nanodot array of 500 μm x 500 μm area, characterized by a complex double-dot unit cell arranged on a rectangular lattice, has been fabricated on self-oxidized Si [1 0 0] substrate by means of electron-beam lithography (EBL) and electron-beam evaporation (EBE). The deposition chamber was maintained at a base pressure of 2×10^{-8} Torr during the evaporation and the lithography was performed for a dose time of 1.0 μs at a beam current of 500 pA. The diameter of the larger and smaller dot of one unit is about 700 nm and 280 nm, respectively. The separation between larger and smaller dot (intra-unit) is about 35 nm, while the inter-unit separation is about 170 nm. The corresponding lattice constants are $a = 1185$ nm and $b = 850$ nm, as shown in the inset of Fig. 1(b). The diameter of the dots and the edge-to-edge separation between the dots show a maximum of ± 5% and ± 10% deviation, respectively.

Dispersion characteristics of thermal SWs in this Py diatomic dot array was recorded by Brillouin light scattering (BLS) technique. Due to the interaction between incident photons and magnons (quanta of SWs), light is scattered inelastically in BLS technique. The BLS spectra were measured and analyzed in the 180° backscattered geometry using a monochromatic solid state laser light (wavelength $\lambda = 532$ nm, power = 130 mW, spot size ≈ 40 μm) and a Sandercock-type (3 + 3) pass tandem Fabry-Perot interferometer (JRS Scientific Instruments). As a consequence of the conservation of momentum during the inelastic scattering, the in-plane transferred wave vector q depends on the incidence angle of light θ according to the equation: $q = (4\pi/\lambda)\sin\theta$. The incident and scattered beams were maintained in a cross polarized geometry during experiment to minimize the phonon contribution to the scattered light. The sample was subjected to an in-plane magnetic field, $H = 1.0$ kOe during the measurements, ensuring magnetic saturation of the sample, as can be inferred from magnetic hysteresis loop [36]. The BLS spectra were measured in the Damon-Eshbach geometry where the bias magnetic field and wave vector are mutually perpendicular, both being in the sample plane. The SW dispersion measurements have been done for two different values of φ, namely φ = 0° and 90°, as shown in Fig. 1(a). We have recorded the spectra for up to two Brillouin Zones (BZs), i.e. $q = 0.73 \times 10^7$ rad/m for φ = 0° and $q = 0.53 \times 10^7$ rad/m for φ = 90°.

3. Theoretical approach and numerical simulations

We have calculated and interpreted the SW excitation spectra and dispersion of the diatomic dot lattice by plane wave method (PWM) [18,27]. In this method the Landau-Lifshitz (LL) equation, i.e. the equation of motion of the magnetization vector $\boldsymbol{M}(\boldsymbol{r},t)$ in space and time is solved under an effective magnetic field $\boldsymbol{H}_{eff}$:

$$\frac{\partial \boldsymbol{M}(\boldsymbol{r},t)}{\partial t} = -\gamma\mu_0 \boldsymbol{M}(\boldsymbol{r},t) \times \boldsymbol{H}_{\text{eff}}(\boldsymbol{r},t) \quad (1)$$

In general $\boldsymbol{H}_{\text{eff}}$ is the sum of several components and can be written as:

$\boldsymbol{H}_{eff} = \boldsymbol{H} + \boldsymbol{H}_{ex} + \boldsymbol{H}_{MS}$, where $\boldsymbol{H}$ is the uniform applied magnetic field, $H_{ex}(r,t) = (\nabla . l_{ex}^2(r)\nabla)m(r,t)$ is the exchange field with exchange length $l_{ex} = \sqrt{2A/\mu_0 M_s^2}$, $\boldsymbol{H}_{MS}$ is the magnetostatic field and A is the exchange stiffness constant. The exchange field and the magnetostatic field are space and time dependent. In the linear approximation, the component of the magnetization vector parallel to the static magnetic field is constant in time, and its magnitude is much greater than that of the perpendicular components. So, $|\boldsymbol{m}(\boldsymbol{r},t)| \ll M_s(\boldsymbol{r})$, where $\boldsymbol{M}(\boldsymbol{r},t) = M_S(\boldsymbol{r})\hat{z} + \boldsymbol{m}(\boldsymbol{r},t)$. In our calculations, we have assumed the static magnetic field to be oriented always along the z axis. Subsequently, all the periodic functions (both in time and space), including the static and dynamic parts of the magnetic fields and magnetization components, are mapped onto the Fourier space using Bloch's theorem [18]. Thus, the LL equation is converted to an algebraic eigenvalue problem, which is solved by standard numerical routines to

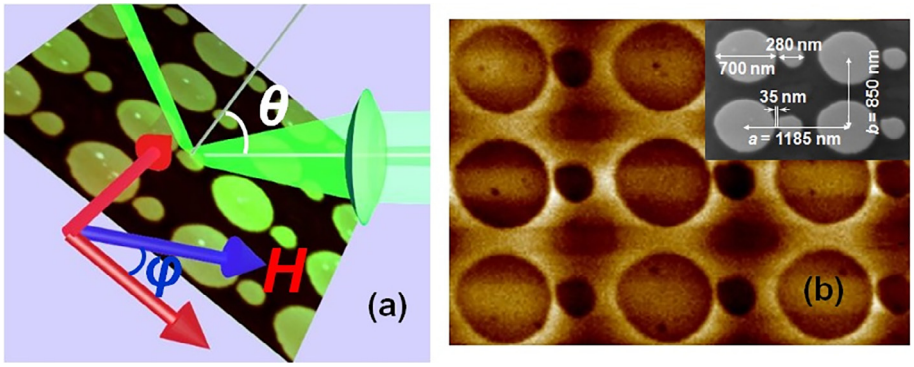

Fig. 1. (a) Schematic of the BLS measurement in backscattered geometry. The incident and scattered beams and the angle θ between them are shown. The in-plane orientation (φ) of the applied bias magnetic field H is also shown. (b) MFM image of the array. The inset shows the SEM image of the sample with the parameters.

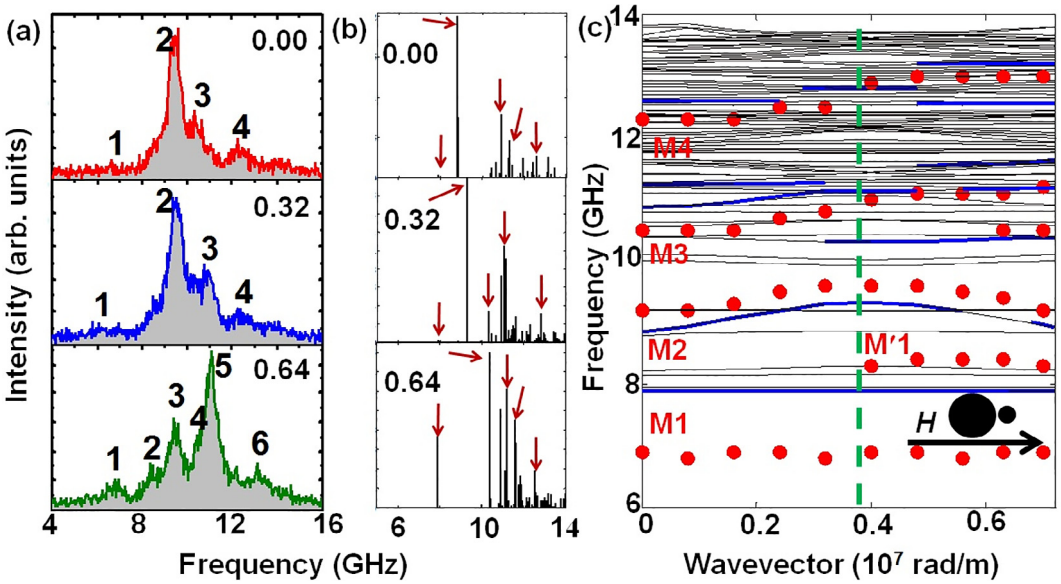

Fig. 2. (a) The Stokes side of BLS spectra taken at different values of the in-plane transferred wave vector q (denoted in units of 10^7 rad/m) for φ = 0°. The spectra are horizontally flipped for convenience. Mode numbers are mentioned for corresponding spectra. (b) Relative values of BLS intensities calculated by PWM for different values of q as shown here. (c) Magnonic band structure for φ = 0°. Thin lines are PWM results. Bold lines emphasize intense excitations as predicted by PWM. Solid circles represent the peaks in the BLS spectra. The dashed vertical line is the boundary of first BZ.

find out the eigenvalues (SW frequencies) and eigenvectors (amplitude of the dynamical component of the magnetization vector) [18,27].

The magnetostatic field is divided into a static ($\boldsymbol{H}_{MS}(\boldsymbol{r})$) and dynamic ($\boldsymbol{h}_{MS}(\boldsymbol{r},t)$) component. The dynamic component of the magnetization vector is dependent on both space and time and has the form: $\boldsymbol{m}(\boldsymbol{r}, t) = \boldsymbol{m}(\boldsymbol{r})e^{i2\pi\nu t}$. The time dependence of the dynamic magnetostatic field has the same form as that of the dynamic component of the magnetization vector, i.e. $\boldsymbol{h}_{\mathrm{MS}}(\boldsymbol{r},t) = \boldsymbol{h}_{\mathrm{MS}}(\boldsymbol{r})\ e^{i2\pi\nu t}$. In the reciprocal space to express the dynamic components of the magnetization and magnetostatic field we use Bloch's theorem, which asserts that a solution of a differential equation with periodic coefficients can be represented as the product of a plane wave with the wave vector $\boldsymbol{q} = (q_y, q_z)$ from the first BZ and a periodic function, which can be expanded into Fourier series:

$$m(r) = \sum_G m_q(G)e^{i(q+G).r} \tag{2}$$

where $\boldsymbol{G} = (G_y, G_z)$ denotes a reciprocal lattice vector of the periodic structure. The saturation magnetization (M_s) and the squared exchange length $l_{ex}^2$are periodic functions of position in MC and hence they can also be mapped onto the reciprocal space using the Fourier transformation formulas:

$$M_s(r) = \sum_G M_s(G)e^{iG.r}$$

$$l_{ex}^2(r) = \sum_G l_{ex}^2(G)e^{iG.r}$$

where the Fourier coefficients $M_s\ (G)$ and $l_{ex}^2(G)$ are determined analytically. The material parameters used were saturation magnetization M_s = 800 emu.cm^{-3}, anisotropy field $H_k = 0$, Lande g-factor $g = 2$ and exchange stiffness constant $A = 1.3 \times 10^{-6}$ erg.cm^{-1}. The value of A was taken from the literature [37], whereas the other parameters were obtained from ref. 36. To avoid any nonphysical frequency values, small but finite values of M_s and A are used for the air gap in between the magnetic materials. We have taken 450 plane waves to ensure a satisfactory convergence of the eigenvalue problem. The square of the modulus of the fundamental harmonics of magnetization determines the intensities calculated from PWM, which is compared with the experimentally measured peak intensities by BLS.

To provide an illustrative demonstration of how the SW propagation occurs in the diatomic nanodot array, we have simulated the SW response to local microwave excitation for two different orientations of the in-plane bias magnetic field using OOMMF software [38]. The micromagnetic simulations have been performed on a 3 × 3 dots matrix after application of a periodic boundary condition. During the simulations the sample is divided into cuboidal cells of dimensions 4 × 4 × 30 nm^3 where the lateral cell size is below the exchange length of Py (≈5.2 nm) to include the exchange interaction effect. The material parameters used in micromagnetic simulations are same as those used in PWM calculation. Initially the static magnetic configuration is obtained by applying a large enough magnetic field to saturate the sample magnetization followed by the reduction of the magnetic field to the bias field value. Then the system was allowed to reach the equilibrium. After we obtain the static magnetic configuration, we apply a time-varying field of "*sinc*" profile (frequency cut-off of 30 GHz) to launch SWs at the centre of the said array. The excitation is applied over a square region of 50 nm width.

4. Results and discussions

Fig. 1(a) schematically depicts the experimental BLS set up in conventional backscattered geometry. To study the magnonic band structure of 2D MCs, we need to change the SW wave vector, as well as its direction on the sample surface. The angle θ is varied by rotating the sample in the vertical plane, thus ensuring the variation of the magnon wave vector q and measurement of SW dispersion along the principal directions of the BZs of 2D MCs. On the other hand, by varying φ, one can study the effect of changing the angle between the applied in-plane magnetic field direction (assumed to be along the average sample magnetization) and the reference axis of the sample. In our experiment, we have studied the wave vector dispersion of the SWs in two different orientations of the in-plane bias magnetic field by varying θ, while fixing φ at 0° or 90°. Fig. 1(b) shows the magnetic force microscopy (MFM) image of the sample measured at remanence. A clear magnetic contrast is observed in the larger dot showing prominent edge demagnetized regions, but no such contrast is observed in the smaller dot.

In Fig. 2(a), we present few representative BLS spectra at varying wave vector for φ = 0° configuration (H = 1 kOe) showing the

evolution of the SW modes with wave vector. The calculated SW spectra for the corresponding wave vectors and the full SW dispersion for this sample at the same bias field configuration are shown in Fig. 2(b) and (c), respectively. In the dispersion presented in Fig. 2(c), the black lines represent the magnonic bands calculated from PWM, wherein the blue bold lines indicate the magnonic bands with large PWM intensity. The experimentally measured BLS intensities are superimposed on the calculated dispersion by red solid circles. The boundary of the first BZ is indicated by the green dotted vertical line. For $\varphi = 0^{\circ}$, the experimentally obtained BLS spectra are characterized by four well defined modes as illustrated in Fig. 2(a). The experimental dispersion within the first BZ show four distinct modes, which are qualitatively reproduced by the PWM calculation. However, the frequency of mode 1 in the experiment does not agree well with theory. At the boundary of the first BZ, another mode M'1 becomes visible in the experiment, whose frequency lies close to the lowest frequency mode with significant intensity in PWM calculation. In addition, another mode gains significant intensity in PWM calculation at the boundary of the first BZ between M2 and M3, which is reproduced in the experiment only near the boundary of the second BZ. Other modes are in good agreement with theory for the whole range of wave vectors. The first mode (M1) is dispersionless, while M2 shows a significant dispersion with mirror symmetry with respect to the first BZ boundary presumably due to zone-folding. On the contrary, M3 and M4 show rather asymmetric dispersion with respect to the first BZ boundary. We will attempt to understand these behaviours by analyzing the SW mode profiles later in this article.

The experimental and theoretical SW spectra along with the SW dispersion for up to two BZs in $\varphi = 90^{\circ}$ orientation of the applied magnetic field are shown in Fig. 3(a)–(c). Experimentally four modes are observed in this orientation. However, the lowest frequency mode (M1) is not theoretically obtained in this orientation. The mode M2 again shows a dispersive nature with mirror symmetry with respect to the boundary of the first BZ but its curvature reduces presumably due to the reduced group velocity of this SW mode in this orientation. The mode M3 is almost dispersionless both in theory and calculation. M4 is also dispersionless within the first BZ both in theory and experiment, while another high intensity mode was visible in PWM calculation between M3 and M4 within the first BZ, which was not resolved experimentally. Interestingly M4 in experiment splits at the boundary of the 1st BZ into two modes (M′4 and M″4) in the second BZ. These two modes are now well reproduced in PWM calculation. Two additional modes gain significant intensity in PWM calculation between M′4 and M″4, which are not resolved in the experiment.

Deeper insight into the SW dynamics is obtained by calculating the SW mode profiles using the PWM, which correspond to the modulus of amplitude of the x-component of the dynamic magnetization, of the relevant experimental modes. Fig. 4(a) and (b) depict the spatial profiles of the SW modes at $q = 0$ (centre of BZ) and $q = \pi/a$ (boundary of the 1st BZ) for $\varphi = 0^{\circ}$ and Fig. 4(c) and (d) depict the same for $\varphi = 90^{\circ}$. For $\varphi = 0^{\circ}$, the calculated mode profile of M1 at $q = 0$ shows a backward volume (BV) magnetostatic SW mode with $m = 3$ with the power distributed over the larger dots in the array in slightly asymmetric manner within each dot. Previously, it was observed that the frequency of M1 is more accurately reproduced in micromagnetic simulations only after incorporation of the edge deformation [36], which could not be done in the PWM calculation. Hence, precise agreements between the experimental and theoretical mode frequencies are not obtained for this mode. We do not observe any substantial changes in the spatial profiles of M1 at $q = \pi/a$. The mode M2 at $q = 0$ again shows a mixed (n)-backward volume and (m)-Damon Eshbach (BV-DE) character in the larger dot with (m, n) as (5, 2). At $q = \pi/a$, this mode transforms to (4, 2). For M3, the mode profile in the larger dot for both $q = 0$ and π/a have mixed BV-DE character with mode numbers (7, 3) but the overall power distribution on different lobes changes. On the other hand, in the smaller dot the mode shows simple BV character with $m = 2$ at both $q = 0$ and π/a. For mode M4, the BV-DE mode transforms from (6, 4) to (4, 5) as q changes from 0 to π/a. For $\varphi = 90^{\circ}$, the magnetic field is directed perpendicular to the diatomic unit and the edge effects become negligible compared to the former orientation, $\varphi = 0^{\circ}$. Hence, the lowest frequency mode M1 is not obtained in the simulation. For M2, we observe BV-like mode with $m = 4$ and 1, in the larger and smaller dot, respectively at $q = 0$. Here, power is equally distributed in both dots. However, at $q = \pi/a$, the mode transforms to BV-DE nature in the

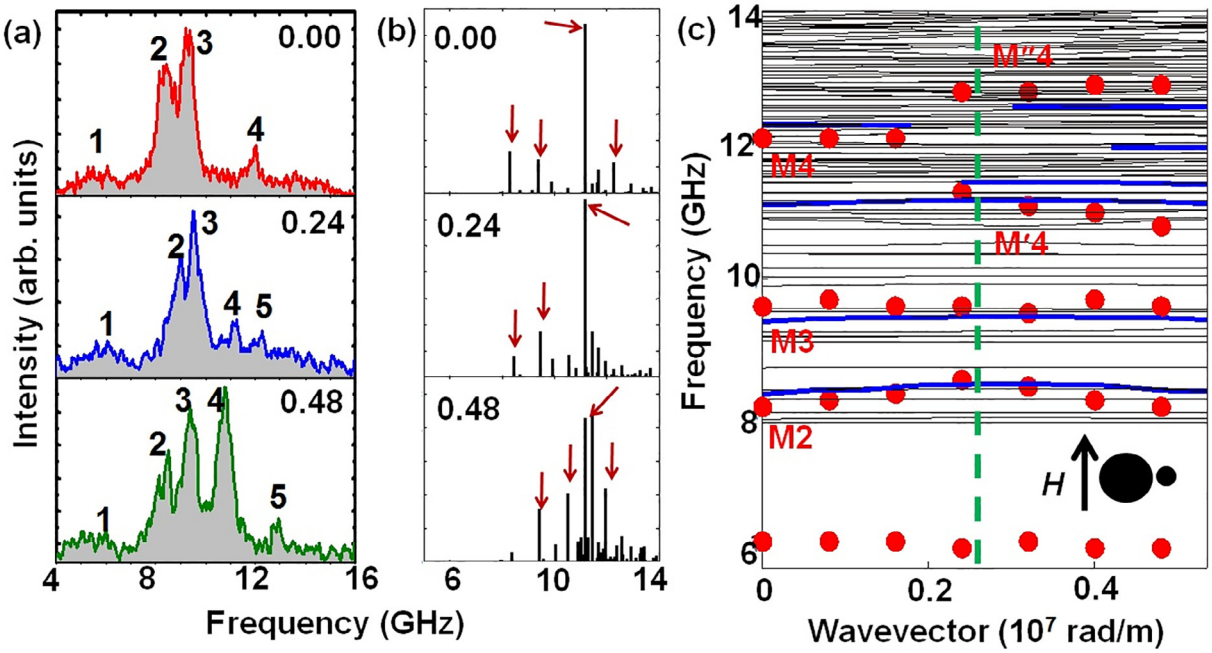

Fig. 3. (a) The Stokes side of BLS spectra taken at different values of the in-plane transferred wave vector q (denoted in units of 10^7 rad/m) for $\varphi = 90^{\circ}$. The spectra are horizontally flipped for convenience. Mode numbers are mentioned for corresponding spectra. (b) Relative values of BLS intensities calculated by PWM for different values of q as shown here. (c) Magnonic band structure for $\varphi = 90^{\circ}$. Thin lines are PWM results. Bold lines emphasize intense excitations as predicted by PWM. Solid circles represent the peaks in the BLS spectra. The dashed vertical line is the boundary of first BZ.

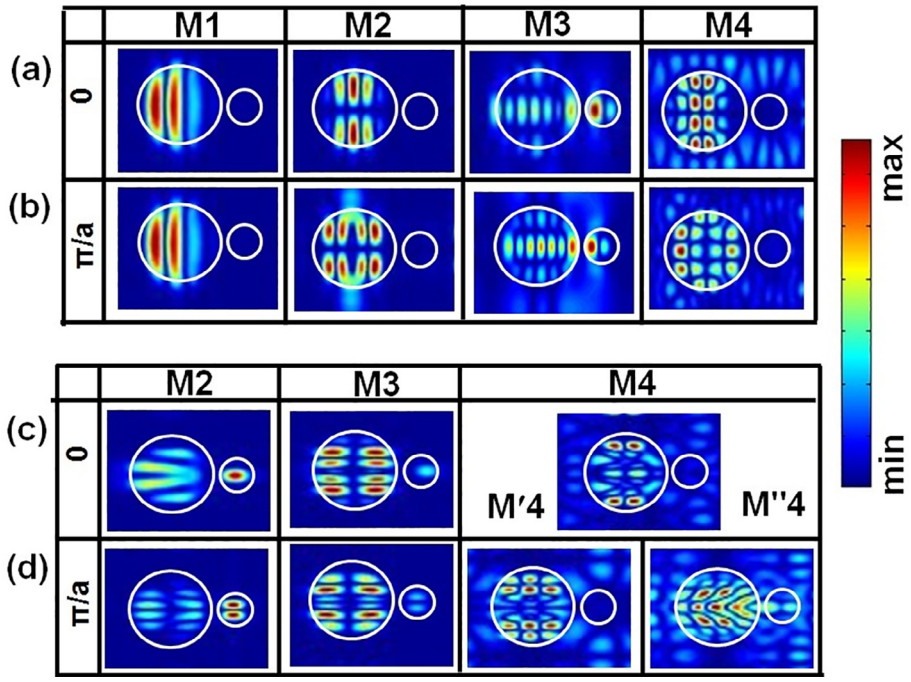

Fig. 4. Spatial profiles of the selected modes for (a) $q = 0$, (b) $q = \pi/a$ at $\varphi = 0^{\circ}$ and (c) $q = 0$, (d) $q = \pi/a$ at $\varphi = 90^{\circ}$.

larger dot with mode numbers (6, 2) and purely BV nature in the smaller dot with $m = 2$. In this case the power is concentrated primarily in the smaller dot. For M3, at $q = 0$, the mode shows a BV-DE character with mode numbers (7, 2) in the larger dots and a BV-like character with $m = 1$ in the smaller dot. It transforms to BV-DE mode with (6, 2) in the larger dot and BV-like mode with $m = 2$ in the smaller dot at $q = \pi/a$. In M3, the power is distributed primarily in the larger dot at both wave vectors. The mode M4 at $q = 0$, shows a mixed BV-DE nature with $m = 9$, $n = 4$. The power is mainly concentrated in the larger dot with comparatively more power at the edges compared to the central regions of the dot. This mode splits into two modes at the boundary of the 1st BZ and the power is again concentrated in the larger dot for both the modes. The lower frequency band M′4 shows mixed BV-DE characteristics ($m = 8$ and $n = 3$). The higher frequency branch M″4 exhibits more complex nature with mixed BV-DE characteristics ($m = 7$, $n = 5$). In the DE geometry, the spatial distribution shows an asymmetric nature presumably due to an interaction with the smaller dot; the latter shows weak power with mode numbers, $m = 1$, $n = 2$.

The usual band diagram representation and the corresponding SW mode profile are not sufficient to provide a deep insight into the propagating nature of the system under investigation. To this end, we have investigated the propagation of the SWs under local excitation for two mutually perpendicular orientations of the applied bias magnetic field. Since the lowest frequency mode, which is strongly affected by the rough edges of the dots, is not well reproduced in the PWM calculations and the highest frequency modes exhibit a complex nature, we mainly focus on the uniform mode (M2 for $\varphi = 0^{\circ}$, M3 for $\varphi = 90^{\circ}$) and the interacting mode (M3 for $\varphi = 0^{\circ}$, M2 for $\varphi = 90^{\circ}$) for this study. The experimental and simulated angular dispersion [39] of the frequency of the uniform mode and the interacting mode shows a nearly constant frequency of the uniform mode with negligible angular dispersion but a sudden transition in the frequency of the interacting mode for $\varphi > 30^{\circ}$. Consequently, the frequency of the interacting mode is greater than the uniform mode for $\varphi < 30^{\circ}$ and less than the uniform mode for $\varphi > 30^{\circ}$. Also, the weaker coupling between the elements flattens the SW dispersion with the wave vector for M3. Fig. 5 shows exemplary simulation results of the SW propagation of the uniform and the interacting modes under local excitation for $\varphi = 0^{\circ}$ and 90°. For this the SW response to microwave excitation, applied at the centre of a 3×3 array using a time-varying field of "*sinc*" profile, has been simulated (Fig. 5(a) and (b) for $\varphi = 0^{\circ}$ and 5(c) and (d) for $\varphi = 90^{\circ}$). Fig. 5(a) reveals that M2 (frequency $\approx$ 9.0 GHz) propagates almost uniaxially in the DE geometry. The mode M3 (frequency $\approx$ 10.5 GHz) exhibits a weak but similar propagation nature in the DE geometry (Fig. 5(b)). This affirms the anisotropic propagation of SWs (in the DE geometry) through the diatomic dot array for $\varphi = 0^{\circ}$. On the contrary, for $\varphi = 90^{\circ}$ the dispersion of M2 (frequency $\approx$ 8.5 GHz) is isotropic throughout the whole lattice (Fig. 5(c)). However, due to its flatter dispersion the energy transfer is less compared to the $\varphi = 0^{\circ}$ case. For M3 (frequency $\approx$ 9.0 GHz) negligible energy gets transferred due to its almost dispersionless behaviour.

To obtain further insight into the origin of the anisotropy of SW propagation for different bias-field orientations, we have further computed the *iso*-frequency contours for the uniform mode and the interacting mode. The *iso*-frequency contours, i.e. the curves of the constant frequency in the wave vector space are wave counterparts of the Fermi surfaces [40]. Important indications regarding the preferential directions of SW propagation are provided by the group velocity, i.e. normal direction to the *iso*-frequency contour, which defines the direction of energy flow within the structure. At a given frequency, the lattice under investigation may behave in a dispersive fashion along certain directions, while being non-dispersive in others. A single *iso*-frequency contour is obtained by fixing the frequency at a fixed value and then scanning q_x from $-\pi/a$ to $+\pi/a$ and q_y from $-\pi/b$ to $+\pi/b$. The dispersion relations of the diatomic dot lattice in the form of *iso*-frequency contours for the M2 and M3 bands in $\varphi = 0^{\circ}$ configuration are presented in Fig. 6(a) and (b). The three-dimensional surface plot of the said magnonic bands, depicting the steepness of dispersion has also been shown in Fig. 6(c) and (d).

The dispersion contours of constant frequency corresponding to both M2 and M3 magnonic bands exhibit anisotropic behaviour in $\varphi = 0^{\circ}$ configuration. In M2, a central minima surrounded by hyperbolic contours are observed, whereas in M3 a 'saddle point' is observed at the centre of the dispersion surrounded again by hyperbolic contours. The surface plots of these two bands, as shown in Fig. 6(c) and (d), confirm that M2 undergoes a steeper dispersion (from 8.8 GHz to

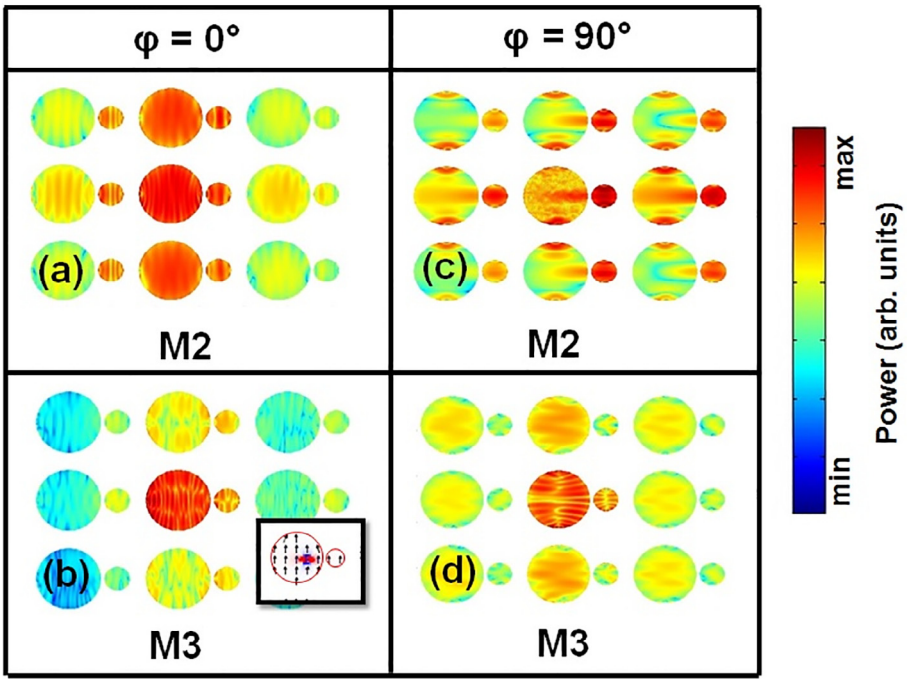

Fig. 5. Power profiles of different SW bands, after application of a local excitation at the central region of the array: (a) M2 at φ = 0°, (b) M3 at φ = 0°, (c) M2 at φ = 90°, (d) M3 at φ = 90°.

9.1 GHz) as opposed to the mode M3 (from 10.39 GHz to 10.42 GHz). On the other hand, Fig. 7 depicts the *iso*-frequency contours and surface plots for M2 and M3 bands in φ = 90° configuration. In this case, the dispersion of M2 band is found to be almost isotropic in nature. But the steepness of dispersion is lowered as opposed to φ = 0° orientation, as observed from the surface plot depicted in Fig. 7c (from 8.34 GHz to 8.44 GHz). On the other hand, the *iso*-frequency contour and the surface plots of M3 band for φ = 90°, as shown in Fig. 7(b) and (d), reveals a very shallow dispersion in the magnonic band. Hence, from the *iso*-frequency contours, we conclude that SW propagation is anisotropic for φ = 0° but becomes nearly isotropic for φ = 90°.

5. Conclusions

In summary, we have performed a combined experimental and numerical study of magnonic band structure and iso-frequency contours in magnetostatically coupled diatomic nanodot arrays with a complex double-dot unit cell. Frequency evolution of several spin eigenmodes as a function of wave vector in two different orientations of the applied in-plane magnetic field (φ = 0° and 90°) has been studied. A steeper dispersion of the uniform mode compared to the interacting mode, whose frequency is blue shifted with respect to the uniform mode, is found in φ = 0° configuration. Due to weaker interaction among the dots, the

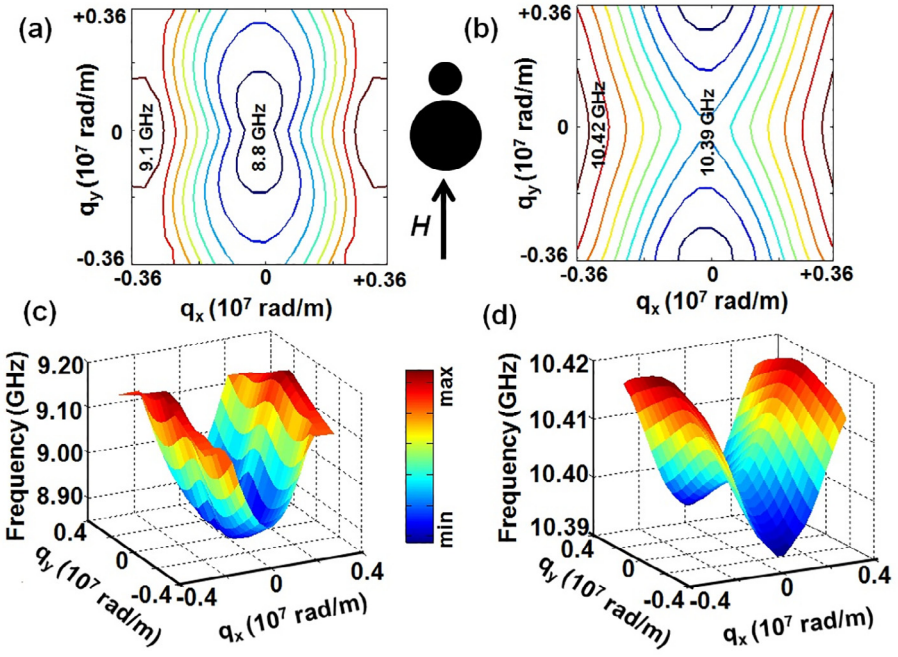

Fig. 6. Iso-frequency contours for (a) M2 and (b) M3 bands and the three-dimensional surface plot of (c) M2 and (d) M3 bands in φ = 0° configuration.

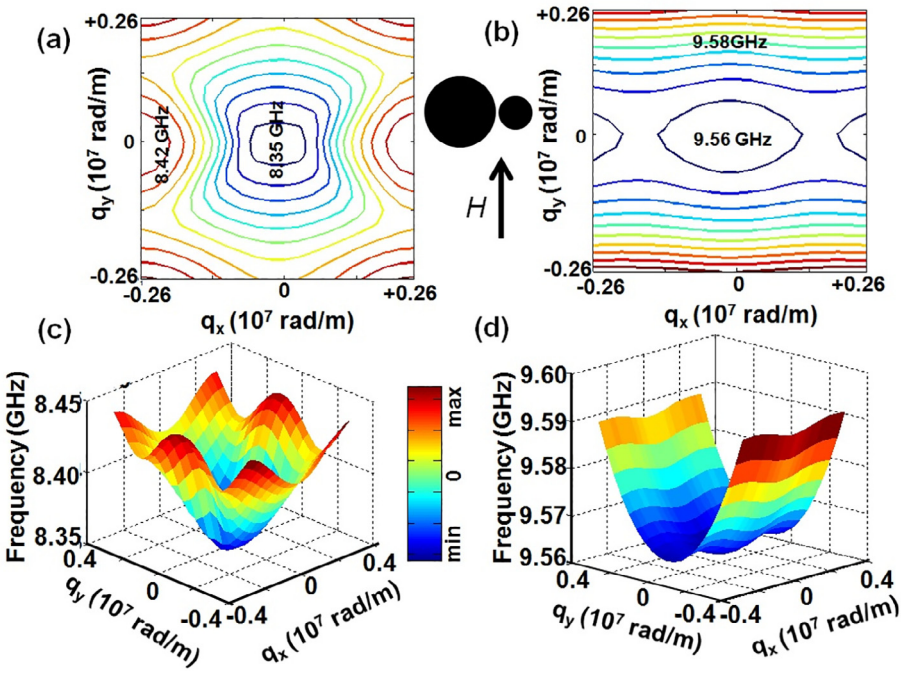

Fig. 7. Iso-frequency contours for the (a) M2 and (b) M3 bands and the three-dimensional surface plot of the (c) M2 and (d) M3 bands in φ = 90° configuration.

dispersion weakens and the nature is reversed for φ = 90°. Here, the red shifted interactive mode is found to be more dispersive than the uniform mode. A detailed micromagnetic investigation using local excitation and the calculated iso-frequency contours from plane-wave method further reveal the anisotropic properties of the SW eigenmodes and its origin. It has been observed that the SW propagation is anisotropic for φ = 0° but becomes nearly isotropic for φ = 90°. The dynamic dipolar coupling between the larger and smaller dots can play a crucial role by affecting the SW dispersion with wave vector for different orientations of the in-plane magnetic field. This work may lead towards the design and understanding of new type of reprogrammable binary magnonic crystal.

Acknowledgement

The authors gratefully acknowledge the financial support from S. N. Bose National Centre for Basic Sciences (grant no. SNB/AB/18-19/211) and the Department of Science and Technology, Government of India (grant No. SR/NM/NS-09/2011(G)). AD, and AKC acknowledge DST, Govt. of India for INSPIRE Fellowship. CB acknowledges CSIR, Government of India, for the senior research fellowship.

Appendix A. Supplementary data

Supplementary data to this article can be found online at https://doi.org/10.1016/j.jmmm.2019.165557.

References

[1] S. Kaka, M.R. Pufall, W.H. Rippard, T.J. Silva, S.E. Russek, J.A. Katine, Nature 437 (2005) 389.
[2] L. Liu, C.F. Pai, D.C. Ralph, R.A. Buhrman, Phys. Rev. Lett. 109 (2012) 186602.
[3] Y.V. Gulyaev, S.A. Nikitov, L.V. Zhivotovskii, A.A. Klimov, P. Tailhades, L. Presmanes, C. Bonningue, C.S. Tsai, S.L. Vysotskii, Y.A. Filimonov, J. Expt. Th. Phys. Lett. 77 (2003) 567.
[4] B. Lenk, H. Ulrichs, F. Garbs, M. Munzenberg, Phys. Rep. 507 (2011) 107.
[5] D.A. Allwood, G. Xiong, C.C. Faulkner, D. Atkinson, D. Petit, R.P. Cowburn, Science 309 (2005) 1688.
[6] S.K. Kim, S.K. Lee, D.S. Han, Appl. Phys. Lett. 95 (2009) 082507.
[7] S. Louis, I. Lisenkov, S. Nikitov, V. Tyberkevych, A. Slavin, AIP Adv. 6 (2016) 065103.
[8] Q. Wang, P. Pirro, R. Verba, A. Slavin, B. Hillebrands, A.V. Chumak, Sci. Adv. 4 (2018) e1701517.
[9] A.V. Chumak, A.A. Serga, B. Hillebrands, Nat. Commun. 5 (2014) 4700.
[10] M. Inoue, A. Baryshev, H. Takagi, P.B. Lim, K. Hatafuku, J. Noda, K. Togo, Appl. Phys. Lett. 98 (2011) 132511.
[11] Z.K. Wang, V.L. Zhang, H.S. Lim, S.C. Ng, M.H. Kuok, S. Jain, A.O. Adeyeye, ACS Nano 4 (2010) 643.
[12] S. Saha, S. Barman, Y. Otani, A. Barman, Nanoscale 7 (2015) 18312.
[13] C. Banerjee, S. Choudhury, J. Sinha, A. Barman, Phys. Rev. Appl. 8 (2017) 014036.
[14] V.V. Kruglyak, A. Barman, R.J. Hicken, J.R. Childress, J.A. Katine, Phys. Rev. B 71 (2005) 220409(R).
[15] S. Neusser, B. Botters, D. Grundler, Phys. Rev. B 78 (2008) 054406.
[16] A. Barman, A. Haldar, Solid State Physics 65 (2014) 1.
[17] S. Tacchi, B. Botters, M. Madami, J.W. Kłos, M.L. Sokolovskyy, M. Krawczyk, G. Gubbiotti, G. Carlotti, A.O. Adeyeye, S. Neusser, D. Grundler, Phys. Rev. B 86 (2012) 014417.
[18] M. Krawczyk, H. Puszkarski, Phys. Rev. B 77 (2008) 054437.
[19] S. Sahoo, S. Mondal, G. Williams, A. May, S. Ladak, A. Barman, Nanoscale 10 (2018) 9981.
[20] G. Gubbiotti, L.L. Xiong, F. Montoncello, L. Giovannini, A.O. Adeyeye, J. Appl. Phys. 124 (2018) 083903.
[21] G. Gubbiotti, G. Carlotti, T. Okuno, T. Shinjo, F. Nizzoli, R. Zivieri, Phys. Rev. B 68 (2003) 184409.
[22] G. Gubbiotti, G. Carlotti, T. Okuno, M. Grimsditch, L. Giovannini, F. Montoncello, F. Nizzoli, Phys. Rev. B 72 (2005) 184419.
[23] S. Tacchi, M. Madami, G. Gubbiotti, G. Carlotti, H. Tanigawa, T. Ono, M.P. Kostylev, Phys. Rev. B 82 (2010) 024401.
[24] S. Tacchi, F. Montoncello, M. Madami, G. Gubbiotti, G. Carlotti, L. Giovannini, R. Zivieri, F. Nizzoli, S. Jain, A.O. Adeyeye, N. Singh, Phys. Rev. Lett. 107 (2011) 127204.
[25] F. Montoncello, S. Tacchi, L. Giovannini, M. Madami, G. Gubbiotti, G. Carlotti, E. Sirotkin, E. Ahmad, F.Y. Ogrin, V.V. Kruglyak, Appl. Phys. Lett. 102 (2013) 202411.
[26] P. Graczyk, M. Krawczyk, S. Dhuey, W.G. Yang, H. Schmidt, G. Gubbiotti, Phys. Rev. B 98 (2018) 174420.
[27] M. Krawczyk, S. Mamica, M. Mruczkiewicz, J.W. Klos, S. Tacchi, M. Madami, G. Gubbiotti, G. Duerr, D. Grundler, J. Phys. D: Appl. Phys. 46 (2013) 495003.
[28] G. Gubbiotti, S. Tacchi, M. Madami, G. Carlotti, Z. Yang, J. Ding, A.O. Adeyeye, M. Kostylev, Phys. Rev. B 93 (2016) 184411.
[29] S. Saha, S. Barman, J. Ding, A.O. Adeyeye, A. Barman, Appl. Phys. Lett. 102 (2013) 242409.
[30] S. Choudhury, S. Saha, R. Mandal, S. Barman, Y. Otani, A. Barman, ACS Appl. Mater. Interfaces 8 (2016) 18339.
[31] V.S. Bhat, D. Grundler, Phys. Rev. B 98 (2018) 174408.
[32] S. Choudhury, S. Barman, Y. Otani, A. Barman, ACS Nano 11 (2017) 8814.
[33] N. Porwal, S. Mondal, S. Choudhury, A. De, J. Sinha, A. Barman, P.K. Datta, J. Phys. D: Appl. Phys. 51 (2018) 055004.
[34] J. Ding, N. Singh, M. Kostylev, A.O. Adeyeye, Phys. Rev. B 88 (2013) 014301.
[35] D. Tripathy, P. Vavassori, J.M. Porro, A.O. Adeyeye, N. Singh, Appl. Phys. Lett. 97 (2010) 042512.

[36] A. De, S. Mondal, C. Banerjee, A.K. Chaurasiya, R. Mandal, Y. Otani, R.K. Mitra, A. Barman, J. Phys. D: Appl. Phys. 50 (2017) 385002.
[37] K. H. J. Buschow, Handbook of Magnetic Materials 18 (Amsterdam: Elsevier), 168 (2009).
[38] M. Donahue, D.G. Porter, OOMMF User's Guide Version 1.0 Interagency Report NISTIR 6376, 1999 (Gaithersburg, MD: National Institute of Standard and Technology) (http://math.nist.gov/oommf).
[39] Supplemental Materials (URL to be provided by the publisher).
[40] D. Kumar, J.W. Kłos, M. Krawczyk, A. Barman, J. Appl. Phys. 115 (2014) 043917.